

Full paper

Phosphine plasma activation of α -Fe₂O₃ for high energy asymmetric supercapacitorsHanfeng Liang^a, Chuan Xia^a, Abdul-Hamid Emwas^b, Dalaver H. Anjum^b, Xiaohe Miao^b, Husam N. Alshareef^{a,*}^a Materials Sciences and Engineering, Physical Sciences and Engineering Division, King Abdullah University of Science and Technology (KAUST), Thuwal 23955-6900, Saudi Arabia^b Core Lab, King Abdullah University of Science and Technology (KAUST), Thuwal 23955-6900, Saudi Arabia

ARTICLE INFO

Keywords:

Hematite

Fe₂O₃

Plasma activation

Supercapacitors

Energy storage

ABSTRACT

We report a phosphine (PH₃) plasma activation strategy for significantly boosting the electrochemical performance of supercapacitor electrodes. Using Fe₂O₃ as a demonstration, we show that the plasma activation simultaneously improves the conductivity, creates atomic-scale vacancies (defects), as well as increases active surface area, and thus leading to a greatly enhanced performance with a high areal capacitance of 340 mF cm⁻² at 1 mA cm⁻², compared to 66 mF cm⁻² of pristine Fe₂O₃. Moreover, the asymmetric supercapacitor devices based on plasma-activated Fe₂O₃ anodes and electrodeposited MnO₂ cathodes can achieve a high stack energy density of 0.42 mW h cm⁻³ at a stack power density of 10.3 mW cm⁻³ along with good stability (88% capacitance retention after 9000 cycles at 10 mA cm⁻²). Our work provides a simple yet effective strategy to greatly enhance the electrochemical performance of Fe₂O₃ anodes and to further promote their application in asymmetric supercapacitors.

1. Introduction

Supercapacitors (SCs), also known as electrochemical capacitors or ultracapacitors, have attracted significant research interest due to their high power density, long cycle lifetime, and fast charge-discharge rate [1,2]. However, to meet the demands of emerging markets including hybrid electric vehicles and next-generation electronic devices, the energy density of SCs needs to be further improved, without sacrificing their power density. According to the equation $E = \frac{1}{2}CV^2$, where E is the energy density, C the capacitance, and V the operation voltage window [3,4], the energy density of SCs can be enhanced by increasing the device capacitance and/or broadening the cell voltage. The latter approach can be achieved by using ionic liquids or organic electrolytes, which normally possess much wider voltage windows (more than 2 V) compared to aqueous electrolytes (limited to 1.23 V due to the water splitting reaction) [5]. However, ionic liquids are costly whereas organic electrolytes are generally poor ionic conductors and not environmentally friendly, making both electrolytes not ideal for SCs. Alternatively, fabrication of asymmetric supercapacitors (ASCs) with aqueous electrolytes provides an effective way to improve the energy density [6]. ASCs typically consist of a cathode and an anode that work in different potential windows, leading to a broadened cell voltage and

thus a higher energy density compared to symmetric SCs. It is noted that the overall performance of ASCs essentially relies on the properties of electrode materials. Enormous efforts have therefore been devoted to exploring new electrode materials and to optimizing their performance [7,8]. Compared to the great achievements that have been made on cathode materials, anode materials however, have long been the bottleneck limiting the practical application of ASCs. Carbon materials are commonly used anodes, which possess excellent cycling performance and good power density, but suffer from low energy density resulting from their low capacitances [9,10]. Alternative electrodes with high capacitance such as Fe₂O₃, VN, MoO_{3-x} have thus been investigated, aiming to improve the energy density of ASCs [11–14].

Among these anode materials, Fe₂O₃ has received growing attention in recent years owing to its earth abundance, high theoretical specific capacitance, and suitable negative potential window [14–21]. Many strategies have been proposed to enhance the performance of Fe₂O₃ anodes, e.g., by delicate nanostructuring to increase the effective surface area [14], by hybridizing with carbon materials or doping to enhance the electric conductivity [15,17,19], or by defect engineering to improve the reactivity [21]. Unfortunately, despite the great progress that has been achieved, the performance of Fe₂O₃ anodes is still unsatisfactory and further improvement is needed. Combining these

* Corresponding author.

E-mail address: husam.alshareef@kaust.edu.sa (H.N. Alshareef).

strategies might further enhance the performance but has rarely been achieved mainly due to the complexity of putting reaction schemes involved in different synthetic methods together.

In this work, we present an “all-in-one” phosphine (PH_3) plasma activation strategy that could simultaneously tune the active surface area, conductivity, and vacancy (defect) concentration and thus significantly boost the performance of Fe_2O_3 anodes. Plasma has been employed as an effective surface modification technique since 1966 [22], which provides a possibility to selectively modify the surface without changing the bulk properties [23,24]. The changes of surface highly depend on the gas type and typical gases used are O_2 , H_2 , N_2 , and Ar [25–29]. The N_2 plasma has recently also been used for the synthesis of metal nitrides [30–34]. While these gases are normal, the use of PH_3 plasma is much less common, which has been so far mostly used for passivation of (In)GaAs semiconductors [35]. We previously demonstrated that PH_3 plasma can be used to convert various precursors into phosphides (e.g. NiCoP , NiFeP , Ni_2P) at low temperatures in a short reaction time [36–39]. Such unique plasma conversion is a powerful and versatile tool that should also work for the synthesis of FeP. It should be pointed out, however, that FeP is a good hydrogen evolution reaction (HER) electrocatalyst with a small onset potential [40], meaning that when it serves as a supercapacitor electrode, the working potential window would likely narrow as compared to Fe_2O_3 , which is undesirable as the narrow potential would lower the energy and power density. Herein, we suggest that PH_3 plasma could be also used to activate the Fe_2O_3 but without changing the bulk phase. We show that the PH_3 plasma activation effectively tunes the active surface area, electric conductivity, as well as defect concentrations, and thus leading to a greatly enhanced performance. Specifically, the PH_3 plasma activated Fe_2O_3 ($\text{Fe}_2\text{O}_3\text{-P}$) can deliver a high areal capacitance of 340 mF cm^{-2} at 1 mA cm^{-2} in $1 \text{ M Na}_2\text{SO}_4$, compared to 66 mF cm^{-2} of pristine Fe_2O_3 . Encouragingly, the ASCs based on $\text{Fe}_2\text{O}_3\text{-P}$ and MnO_2 achieved a high stack energy density of $0.42 \text{ mW h cm}^{-3}$ at a stack power density of 10.3 mW cm^{-3} along with good stability.

2. Experimental section

2.1. Preparation of plasma treated Fe_2O_3 nanorods

FeOOH nanorods were first synthesized by hydrothermal reacting $0.4 \text{ g FeCl}_3\cdot\text{H}_2\text{O}$ with $0.24 \text{ g Na}_2\text{SO}_4$ at 120°C for 6 h using carbon cloth as substrate. The Fe_2O_3 nanorods on carbon cloth were obtained by thermal annealing the FeOOH precursor at 450°C in air for 3 h . The resulted porous Fe_2O_3 nanorods were then subjected to PH_3 plasma activation at 300°C for 1 h to get PH_3 activated Fe_2O_3 ($\text{Fe}_2\text{O}_3\text{-P}$) nanorods. The conditions used for plasma activation were a PH_3/He (1:9 in volume) flux of 50 sccm , a power of 200 W and a base pressure of 800 mTorr .

2.2. Preparation of MnO_2 nanosheets

The MnO_2 nanosheets were prepared on a carbon cloth by electrodeposition at 1.0 V for 2 min using 0.1 M manganese acetate and 0.1 M sodium sulfate as electrolyte. The electrodeposition was performed using a three-electrode configuration, where a Pt plate was used as the counter electrode, an Ag/AgCl electrode as the reference electrode and a carbon cloth as the working electrode.

2.3. Material characterization

X-ray diffraction (XRD) measurements were performed using a Bruker D8 Advanced X-ray diffractometer using $\text{Cu K}\alpha$ radiation. Rietveld XRD refinement was performed using the MAUD program (Materials Analysis Using Diffraction) [41]. Raman spectra were recorded on a Horiba LabRAM HR spectrometer. X-ray photoelectron spectroscopy (XPS) data were collected using an Amicus ECSA 3400

spectrometer. The morphology and structure were characterized using a FEI Nova Nano 630 scanning electron microscopy (SEM) and a FEI Titan 80-300ST (300 kV) transmission electron microscopy (TEM). Energy-filtered TEM (EFTEM) mode of TEM was utilized to generate the elemental maps. These experiments were completed by using a post-column energy-filter of model GIF Quantum 966 from Gatan, Inc. We selected energy-loss edges P-L23 (132 eV), O-K (532 eV), and Fe-L23 (708 eV) for generating the maps of P, O, and Fe, respectively. Moreover, the so-called 3-window method was employed during the mapping experiments. Electron paramagnetic resonance (EPR) spectra were recorded using continuous wave Bruker EMX PLUS spectrometer equipped with standard resonator at room temperature employing 25 dB microwave attenuation with 5 G modulation amplitude and 100 kHz modulation frequency. The UV-vis spectra were recorded using a Perkin Elmer Lambda 45 spectrophotometer and Teflon-stopped quartz cells with a path length of 1 cm .

2.4. Electrochemical measurements

The electrochemical studies of individual electrodes were carried out in $1 \text{ M Na}_2\text{SO}_4$ electrolyte using a three-electrode configuration, where a Pt wire and a Ag/AgCl electrode served as counter electrode and reference electrode, respectively. Whereas for full cell measurements, $1 \text{ M Na}_2\text{SO}_4$ was used as electrolyte; $\text{Fe}_2\text{O}_3\text{-P}$ and MnO_2 on carbon cloth were used as the negative electrode and positive electrode to assemble an asymmetric supercapacitor (ASC), respectively. The area of two electrodes was optimized prior to the fabrication of ASC according to the following equation:

$$C_+A_+V_+ = C_-A_-V_- \quad (1)$$

where A is the area, C the areal capacitance and V the voltage window for the positive (+) and negative (-) electrodes, respectively. For a typical device, the stack thickness was $\sim 0.8 \text{ mm}$. Cyclic voltammetry (CV), galvanostatic charge-discharge (GCD) tests, and electrochemical impedance spectroscopy (EIS) measurements were conducted on a Bio-Logic VMP3 potentiostat.

2.5. Calculations

The energy density was calculated from the GCD curves as following:

$$E = \frac{I \int V(t) dt}{Vol} \quad (2)$$

where I is the constant current for charge-discharge, V the voltage window, t the discharge time, Vol the total volume of the entire asymmetric supercapacitors. The power density was calculated according to

$$P = E/t \quad (3)$$

The capacitance can be calculated as

$$C = 2E/V^2 \quad (4)$$

3. Results and discussion

The Fe_2O_3 nanorod arrays on carbon cloth were first synthesized by thermally annealing FeOOH precursor (see Fig. S1 and Experimental section in Supporting information) at 450°C for 2.5 h . Scanning electron microscopy (SEM) and transmission electron microscopy (TEM) observation reveal that the as-obtained Fe_2O_3 inherits the morphology of FeOOH with dense nanorods around 65 nm in diameter vertically aligned on the skeleton of carbon cloth (Fig. 1a and b). High-resolution TEM (HRTEM) image further confirms the phase as the lattice spacing of 0.27 nm matches well with the d -spacing of (10–14) planes of Fe_2O_3 (Fig. 1c). The selected area electron diffraction (SAED) pattern further

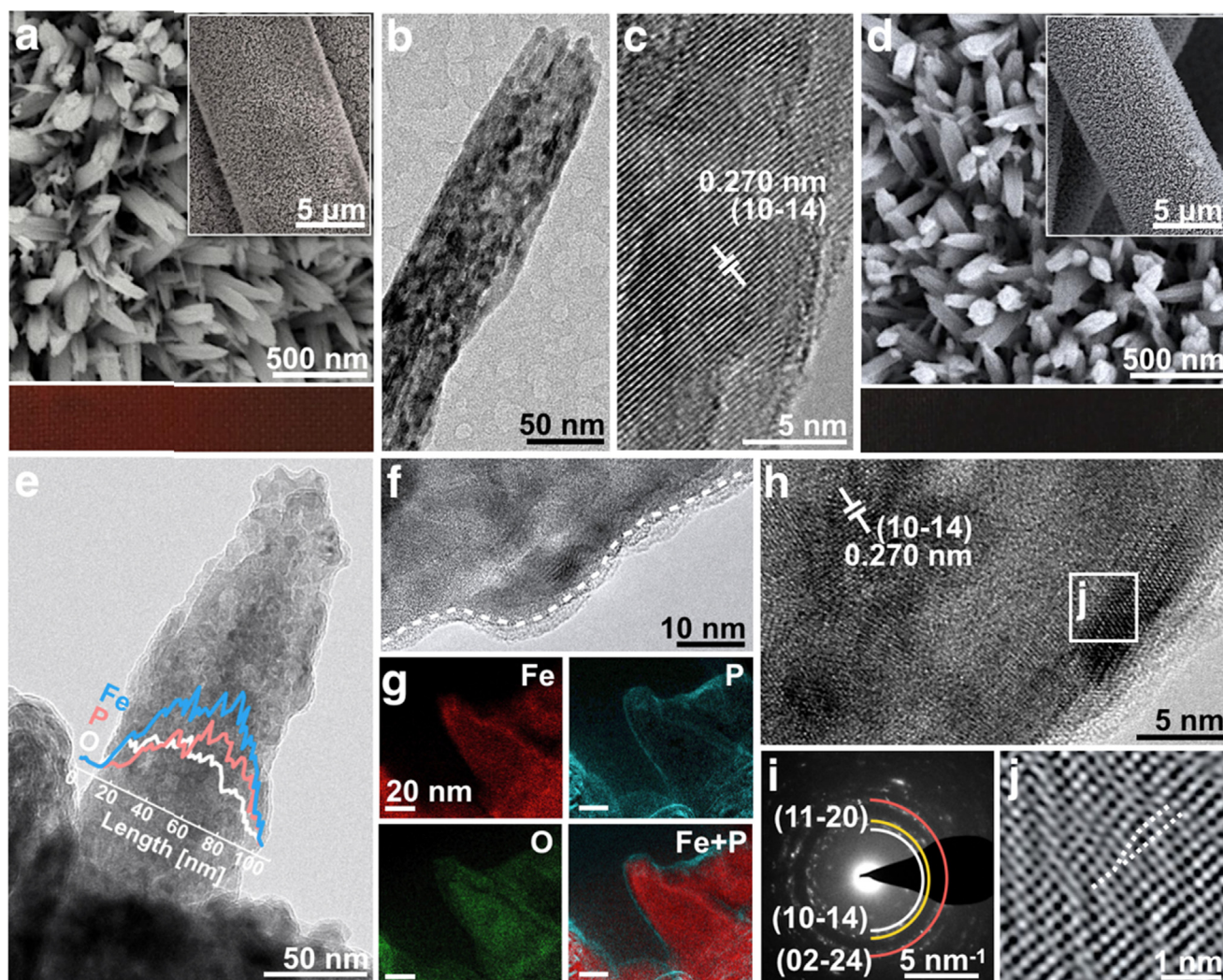


Fig. 1. Morphological characterization of Fe_2O_3 and $\text{Fe}_2\text{O}_3\text{-P}$ nanorods. (a) SEM image and digital photograph, (b) TEM, and (c) HRTEM images of Fe_2O_3 nanorods. (d) SEM image and digital photograph, (e), (f) TEM images, (g) EELS elemental maps, (h) HRTEM image, (i) SAED pattern of $\text{Fe}_2\text{O}_3\text{-P}$ nanorods, and (j) Inverse Fourier-filtered image of the square marked area in h. The inset of e shows the EDS line scan of elemental signal profiles.

confirms the phase of the as-obtained nanorods (Fig. S2, Supporting information). The Fe_2O_3 nanorods were then subjected to a PH_3 plasma activation for 1 h to get the $\text{Fe}_2\text{O}_3\text{-P}$ nanorods. As shown in Fig. 1d, the nanorod morphology is well retained after the plasma process while the carbon cloth turns black (bottom of Fig. 1d), indicating the bandgap of the material has changed. This is further confirmed by the UV–vis measurement, which shows that the bandgap of the pristine Fe_2O_3 decreases from 2.25 to 1.80 eV after plasma treatment (Fig. S3, Supporting information). TEM image further reveals the porous nanorod morphology (Fig. 1e). A close observation shows that there is a ~ 1.8 nm thick amorphous layer on the surface (the crystalline-amorphous interface is indicated by a dash line, see Fig. 1f), which consists of Fe phosphide/phosphate as will be discussed later. The energy dispersive X-ray spectroscopy (EDS) line scan profiles (inset of Fig. 1e) further confirm the existence of Fe, O, and P in the nanorods. The electron energy loss spectroscopy (EELS) elemental maps (Fig. 1g) clearly indicates a P-rich surface layer that could be metal phosphide/phosphate. However, the lattice spacing of 0.27 nm (Fig. 1h) for $\text{Fe}_2\text{O}_3\text{-P}$ as well as the SAED pattern (Fig. 1i, see Fig. S4, Supporting information for the selected area that was used for the diffraction imaging) reveal that the phase remains Fe_2O_3 , which suggests that the plasma activation does not change the bulk material. The plasma activation also introduces abundant of defects such as line dislocations

(Fig. 1j), which would provide more active sites for electrochemical reactions [42].

We further carried out structural characterizations of Fe_2O_3 and $\text{Fe}_2\text{O}_3\text{-P}$ nanorods. The X-ray diffraction (XRD) patterns of these two samples can be indexed into the hexagonal hematite phase (Fig. 2a), again confirming no phase transformation during the plasma process. We noted that there are two small diffraction peaks around 31° and 55° are observed in both samples, which should be from the $\gamma\text{-Fe}_2\text{O}_3$ (#25-1402) formed during the thermal annealing. Though the XRD patterns are identical, the cell parameters obtained from Rietveld XRD refinements are sensibly different from each other (Fig. S5, Supporting information). This result suggests that the plasma treatment has affected the crystal structure of Fe_2O_3 . The EDS spectra show that P is introduced to the Fe_2O_3 after plasma activation (Fig. 2b), which might mainly exist on the surface as iron phosphates and phosphides as revealed by X-ray photoelectron spectroscopy (XPS) analysis. For pristine Fe_2O_3 , the Fe 2p spectrum shows two distinguished peaks ($2p_{3/2}$ at 711.0 eV and $2p_{1/2}$ at 724.6 eV, $\Delta = 13.6$ eV) along with their associated satellite peaks (Fig. 2c), which match well with those reported for hematite [43,44]. Whereas for $\text{Fe}_2\text{O}_3\text{-P}$, peak fitting analysis suggests two new distinct iron species, which can be identified as Fe^{3+} in phosphates (Fe-PO_4 , $2p_{3/2}$ peak at 713.6 eV) and $\text{Fe}^{\delta+}$ (δ is likely very close to 0) in phosphides (Fe-P , $2p_{3/2}$ peak at 707.7 eV), respectively

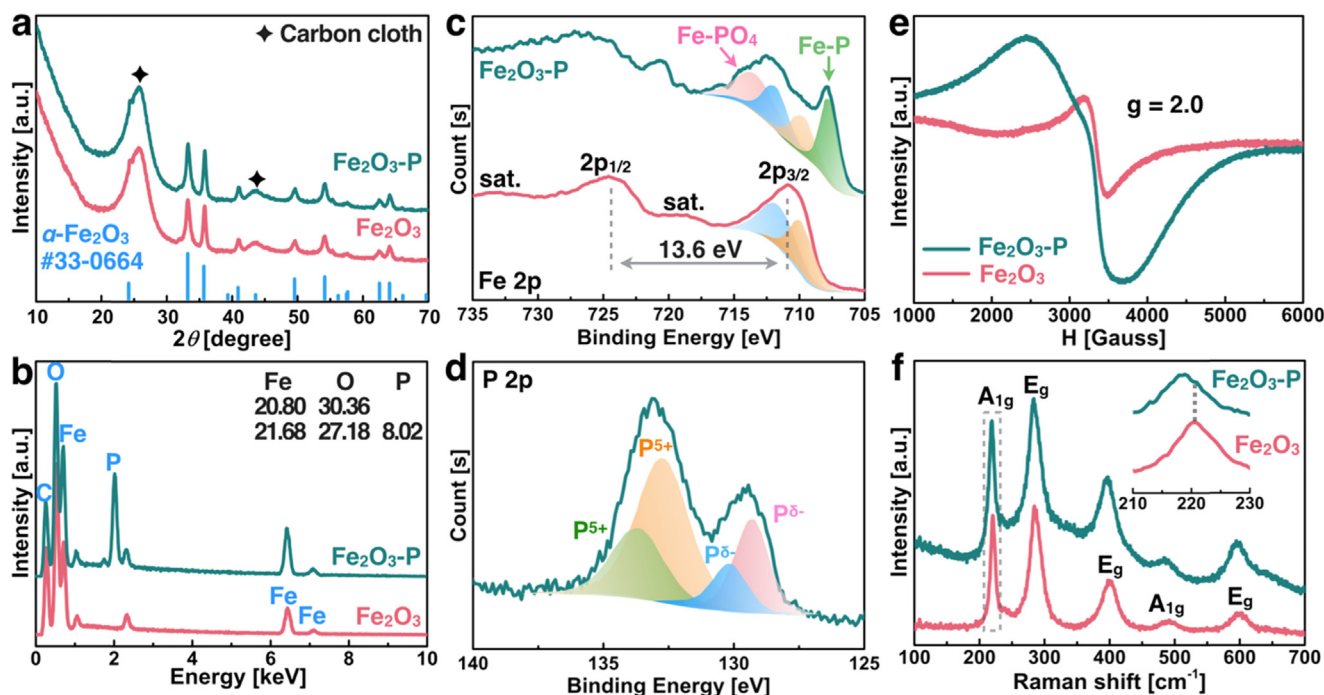


Fig. 2. Structural characterization of Fe_2O_3 and $\text{Fe}_2\text{O}_3\text{-P}$ nanorods. (a) XRD patterns, (b) EDS spectra, and (c) Fe 2p XPS spectra of Fe_2O_3 and $\text{Fe}_2\text{O}_3\text{-P}$. (d) P 2p XPS spectrum of $\text{Fe}_2\text{O}_3\text{-P}$ nanorods. (e) EPR spectra and (f) Raman spectra of Fe_2O_3 and $\text{Fe}_2\text{O}_3\text{-P}$. The inset of f shows the zoom-in Raman spectra of the marked area.

[37]. Further, the P 2p spectrum of $\text{Fe}_2\text{O}_3\text{-P}$ (Fig. 2d) also suggests the existence of P^{5+} (Fe-PO_4) and P^{5-} (Fe-P) [45], in agreement with our TEM observation (see Fig. 1f and h). To probe the effects of plasma activation on the properties of $\text{Fe}_2\text{O}_3\text{-P}$, we then performed electron paramagnetic resonance (EPR) analysis, a technique that is sensitive to unpaired electrons and has been used to reveal the concentration of O vacancies in Fe_2O_3 [21]. As shown in Fig. 2e, the EPR spectra of both Fe_2O_3 and $\text{Fe}_2\text{O}_3\text{-P}$ show a main signal at $g = 2.0$, which can be assigned to Fe^{3+} ions coupled by exchange interactions [46,47]. Compared to Fe_2O_3 , the EPR spectrum of $\text{Fe}_2\text{O}_3\text{-P}$ is much broader, suggesting that there are interactions between Fe^{3+} and other low valance Fe species (e.g., Fe^{2+}). The peak intensity is also much higher, which indicates more O vacancies (defects) present in $\text{Fe}_2\text{O}_3\text{-P}$ [21]. Raman spectra were also collected and all the Raman peaks can be indexed to $\alpha\text{-Fe}_2\text{O}_3$ (Fig. 2f). Note that a negative shift in peaks for $\text{Fe}_2\text{O}_3\text{-P}$ is observed, suggesting an increased concentration of O vacancies. Similar phenomenon has also been reported for N_2 -annealed Fe_2O_3 [21]. Further, an induced strain between surface longer Fe-P bonds and Fe-O is expected (an average length of 2.369 Å for Fe-P bonds compared to 2.009 Å for Fe-O bonds). The lengthening of the interionic distance is correlated to a decrease of the force constants between pairs of ions, also results in a negative shift. These results further demonstrate that the plasma activation doesn't change the main phase of bulk Fe_2O_3 , but creates more O vacancies (defects), which would improve the intrinsic conductivity and promote the reactivity of Fe_2O_3 . Moreover, the in situ generated surface phosphates and phosphides could also increase the effective surface area and participates in the surface faradaic reactions as will be demonstrated later.

We thus studied the electrochemical performance of Fe_2O_3 and $\text{Fe}_2\text{O}_3\text{-P}$ using a three-electrode configuration in 1 M Na_2SO_4 electrolyte. Fig. 3a compares the cyclic voltammograms (CVs) of carbon cloth, Fe_2O_3 , and $\text{Fe}_2\text{O}_3\text{-P}$ recorded at 100 mV s^{-1} . As expected, the $\text{Fe}_2\text{O}_3\text{-P}$ electrode exhibits a substantially higher current density than that of pristine Fe_2O_3 electrode, indicating a great enhancement in pseudocapacitive performance due to the plasma activation. The quasi-rectangular shape further suggests that the $\text{Fe}_2\text{O}_3\text{-P}$ electrode is charged/discharged at a pseudo-constant rate over the entire voltammetric

cycles with a rapid faradaic reaction between alkaline cations (e.g., Na^+ , Li^+) [48,49]. Such phenomenon is likely due to improved conductivity and the fast diffusion of ions during charge-discharge process [50]. The CV for $\text{Fe}_2\text{O}_3\text{-P}$ retains the rectangular shape even at 200 mV s^{-1} (Fig. S6, Supporting information), implying an ideal capacitive performance. Fig. 3b displays the galvanostatic charge-discharge (GCD) profiles of Fe_2O_3 and $\text{Fe}_2\text{O}_3\text{-P}$ electrodes collected at 2 mA cm^{-2} (see Fig. S6, Supporting information) for GCD profiles at different current densities). Larger covered area can be identified for $\text{Fe}_2\text{O}_3\text{-P}$, suggesting a higher capacitance. Indeed, the $\text{Fe}_2\text{O}_3\text{-P}$ can deliver a much higher areal capacitance of 340 mF cm^{-2} (369 F g^{-1}) at 1 mA cm^{-2} , compared to 66 mF cm^{-2} (86 F g^{-1}) of pristine Fe_2O_3 (Fig. 3c). Note that this capacitance is considerably higher than that reported for most Fe_2O_3 -based anodes, such as Fe_2O_3 nanotubes (180 mF cm^{-2} at 1 mA cm^{-2}) [14], oxygen-deficient Fe_2O_3 nanorods (277 mF cm^{-2} at 10 mV s^{-1}) [21], Fe_2O_3 @PANI nanowires ($\sim 52 \text{ mF cm}^{-2}$ at 1 mA cm^{-2}) [16], Fe_2O_3 @PPy nanotubes (207 mF cm^{-2} at 1 mA cm^{-2}) [20], and Fe_3O_4 @ Fe_2O_3 nanorods (232 F g^{-1} at 5 mV s^{-1}) [18] (Table S1, Supporting information). The $\text{Fe}_2\text{O}_3\text{-P}$ anodes also possess a good cycling stability with 83% capacitance retention after 5000 cycles at a high current density of 20 mA cm^{-2} (Fig. 3d). The SEM characterization after cycling shows that the overall nanorod morphology remains (Fig. S7, Supporting information). The EDS spectrum and the EELS elemental mapping further reveal the existence of Fe, O, and P, suggesting the surface phosphide/phosphate layer is stable for at least 5000 cycles of electrochemical test. These results confirm the efficacy of our strategy for greatly enhancing the performance of Fe_2O_3 anodes through surface plasma activation.

In an effort to understand the origin of the greatly enhanced performance, we first carried out the electrochemical impedance spectroscopy (EIS) analysis. The result reveals that the charge transfer resistance of $\text{Fe}_2\text{O}_3\text{-P}$ is much smaller than that of Fe_2O_3 (Fig. 3e), indicating the improved conductivity of Fe_2O_3 after plasma activation. The abundant O vacancies (see Fig. 1e) not only improve the conductivity but also provide additional active sites for redox reactions [21]. Further, the plasma treatment has introduced phosphates/phosphides to the surface. The partial replacement of O with P on the

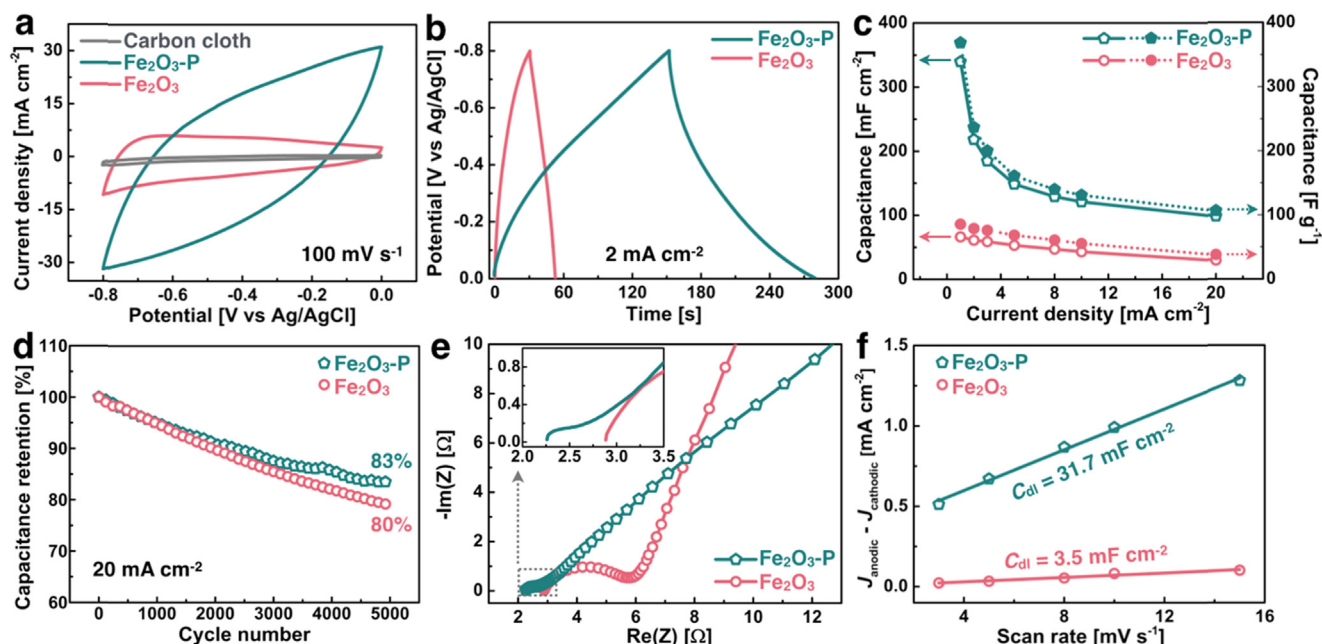


Fig. 3. Comparison of electrochemical performance of Fe₂O₃ and Fe₂O₃-P nanorods in 1 M Na₂SO₄. (a) CV curves at a scan rate of 100 mV s⁻¹. (b) CD profiles at a current density of 2 mA cm⁻². (c) Capacitance plotted against current density. (d) Cycling performance at 20 mA cm⁻². (e) Nyquist plots. (f) Difference in current density plotted against scan rate showing the extraction of the double-layer capacitance.

surface would result in a system with less number of electrons, hence shifting the fermi level to valence bands, which leads to a narrower bandgap, i.e., an improved conductivity (also see the UV-vis spectra in Fig. S3). We also measured the double layer capacitances (C_{dl}) and estimated the electrochemically active surface areas (ECSAs) of the electrodes (CV curves used for the estimation of C_{dl} can be found in Fig. S8, Supporting information) [51,52]. The result shows that the ECSA of Fe₂O₃-P is 8 times larger than that of Fe₂O₃ (Fig. 3f). Such dramatic increase in effective surface area would promote the ion diffusion and provide more active sites. Further, it is noted that the reactivity of electrode materials is associated with the chemical bonds and electronic environments [53]. The covalent-ionic bond character can be evaluated according to following equation:

$$\text{Covalent character (\%)} = \exp[-0.25(X_a - X_c)^2] \quad (5)$$

where X_a and X_c represent electronegativity value of anion and cation, respectively. Therefore, the covalent characters of Fe-O and Fe-P can be calculated as 52.3% and 96.7%, respectively ($X_{Fe} = 1.83$, $X_P = 2.19$, and $X_O = 3.44$). The high covalency degree of Fe₂O₃-P suggests the electrons in 3d orbitals of Fe have higher energies. Further, as we discussed earlier, the Fe-P bonds are generally longer than that of Fe-O bonds, together with the high covalency degree, the activation energy barrier for the redox reactions would be much smaller than that for pristine Fe₂O₃, leading to an enhanced surface reactivity. It is also worth mentioning that Ni/Co phosphates and phosphides have already shown good electrochemical performance as SC electrodes [38,54–56]. It is expected that Fe phosphates/phosphides are also involved in the surface faradaic reactions and contribute to the performance. Moreover, the Fe phosphates/phosphides layer is ultrathin (~1.8 nm, see Fig. 1f) and is thus expected not to have significant activity for HER. Indeed, an increase in surface Fe phosphates/phosphides amount, e.g., by prolonging the plasma activation time, leads to worse capacitive performance as the operational potential window is narrowed due to the strong hydrogen evolution catalyzed by Fe phosphides (Fig. S9, Supporting information) [57,58]. Interestingly, the plasma treated carbon cloth (under the same plasma conditions) shows almost the same performance as the pristine one (Fig. S10, Supporting information), further confirming the enhancement we observed in Fe₂O₃-P

should be due to the synergy between Fe and P as we discussed earlier. These results suggest that the plasma activation could serve as an effective and efficient strategy for enhancing the pseudocapacitive performance of Fe₂O₃ anodes.

Encouraged by the high performance achieved on Fe₂O₃-P anodes, we further assembled ASC devices using Fe₂O₃-P and MnO₂ nanosheets as negative and positive electrodes, respectively. The MnO₂ nanosheet arrays were synthesized by electrodeposition and can deliver a capacitance of 221 mF cm⁻² at 1 mA cm⁻² in 1 M Na₂SO₄. The detailed characterization of MnO₂ nanosheets can be found in Fig. S11, Supporting information. Prior to assembling the ASCs, the charges of Fe₂O₃-P and MnO₂ electrodes are balanced and the optimized areal ratio is about 1:1.5 (see Fig. 4a and details in experimental section, Supporting information). Fig. 4b displays the CV curves of Fe₂O₃-P//MnO₂ ASC device recorded at different scan rates from 10 to 200 mV s⁻¹ within the voltage window of 0–1.6 V. All the CV curves present a quasi-rectangular shape and are highly symmetric, reflecting a good reversibility and typical capacitive behavior. The symmetric GCD profiles with triangular shapes further confirm the superior capacitive performance of our assembled ASC devices (Fig. 4c). We further calculated the energy density and power density of our devices and the results are summarized as Ragone plots in Fig. 4d and e. Impressively, our Fe₂O₃-P//MnO₂ ASC device can achieve a high stack energy density (based on the volume of entire device) of 0.42 mWh cm⁻³ at a stack power density of 10.3 mW cm⁻³, corresponding to a gravimetric energy density of 57.3 Wh kg⁻¹ at 1404 W kg⁻¹, and can still maintain 0.14 mWh cm⁻³ (19.5 Wh kg⁻¹) at 258.1 W cm⁻³ (35,097 W kg⁻¹). Though the device performance may vary with the electrode material preparation methods and the electrochemical testing conditions, the activity of our devices outperforms most of the recently reported iron oxides-based ASCs under similar testing conditions (see comparison in Fig. 4d and e). Besides the high energy and power densities, our Fe₂O₃-P//MnO₂ ASC also shows good cycling performance with 88% capacitance retention after 9000 cycles at a high current density of 10 mA cm⁻² (Fig. 4f).

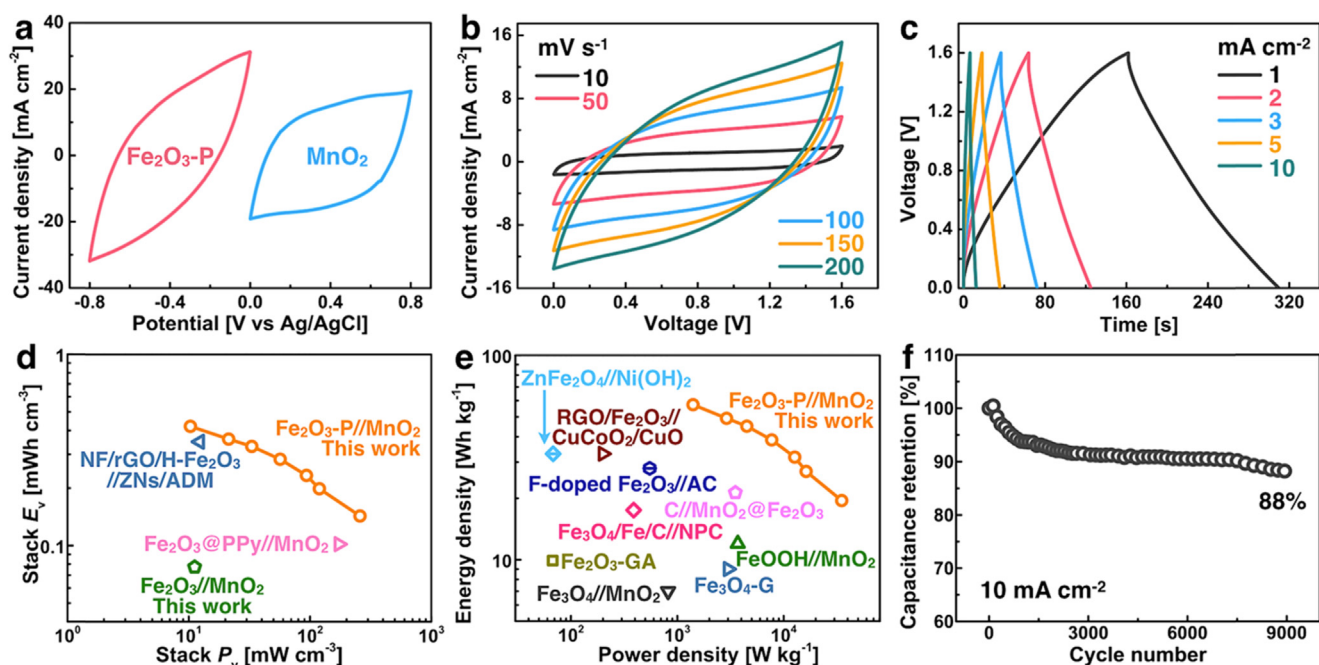


Fig. 4. Electrochemical performance of Fe₂O₃-P/MnO₂ ASCs. (a) CV curves of Fe₂O₃-P, MnO₂ and carbon cloth electrodes collected at 100 mV s⁻¹. (b) CV curves at various scan rates. (c) CD curves at various current densities. (d,e) Ragone plots of the optimized Fe₂O₃-P/MnO₂ ASCs along with other recently reported high-performance ASCs for comparison. (f) Cycling performance at 10 mA cm⁻². Reference cited in d and e: NF/rGO/H-Fe₂O₃//ZnS/ADM [59], ZnFe₂O₄//Ni(OH)₂ [60], RGO/Fe₂O₃//CuCoO₂/CuO [61], F-doped Fe₂O₃//AC [15], C//MnO₂@Fe₂O₃ [62], Fe₃O₄/Fe/C/NPC [63], Fe₂O₃-GA [64], FeOOH//MnO₂ [65], Fe₃O₄-G [66], and Fe₃O₄//MnO₂ [67].

4. Conclusion

In summary, we have presented a new PH₃ plasma activation strategy to significantly boost the capacitive performance of Fe₂O₃ anodes for high-performance ASCs. The plasma treatment doesn't change the bulk phase of Fe₂O₃, however, it effectively tunes the conductivity, active surface area, and defects concentration. As a result, a *fivefold* enhancement in areal capacitance is achieved for the plasma functionalized Fe₂O₃ (340 mF cm⁻² at 1 mA cm⁻²) when compared with the pristine Fe₂O₃ (66 mF cm⁻²). The capacitance of Fe₂O₃-P is among the highest numbers reported for Fe₂O₃ electrodes. Furthermore, the ASC devices consist of Fe₂O₃-P and MnO₂ electrodes achieve a high stack energy density of 0.42 mW h cm⁻³ (57.3 W h kg⁻¹) at a stack power density of 10.3 mW cm⁻³ (1404 W kg⁻¹) along with good stability, outperforming most of the iron oxides-based ASCs. The new plasma activation may serve as a general strategy for enhancing the electrochemical performance of oxides in supercapacitors and many other applications.

Acknowledgements

Research reported in this publication was supported by King Abdullah University of Science and Technology (KAUST).

Appendix A. Supporting information

Supplementary data associated with this article can be found in the online version at <http://dx.doi.org/10.1016/j.nanoen.2018.04.032>.

References

- [1] P. Simon, Y. Gogotsi, Materials for electrochemical capacitors, *Nat. Mater.* 7 (2008) 845–854.
- [2] A. Vlad, N. Singh, C. Galande, P.M. Ajayan, Design considerations for unconventional electrochemical energy storage architectures, *Adv. Energy Mater.* 5 (2015) 1402115.
- [3] M.D. Stoller, R.S. Ruoff, Best practice methods for determining an electrode material's performance for ultracapacitors, *Energy Environ. Sci.* 3 (2010) 1294–1301.
- [4] C. Peng, S. Zhang, X. Zhou, G.Z. Chen, Unequalisation of electrode capacitances for enhanced energy capacity in asymmetrical supercapacitors, *Energy Environ. Sci.* 3 (2010) 1499–1502.
- [5] L.L. Zhang, X. Zhao, Carbon-based materials as supercapacitor electrodes, *Chem. Soc. Rev.* 38 (2009) 2520–2531.
- [6] M. Zhi, C. Xiang, J. Li, M. Li, N. Wu, Nanostructured carbon-metal oxide composite electrodes for supercapacitors: a review, *Nanoscale* 5 (2013) 72–88.
- [7] G.F. Chen, X.X. Li, L.Y. Zhang, N. Li, T.Y. Ma, Z.Q. Liu, A porous perchlorate-doped polypyrrole nanocoating on nickel nanotube arrays for stable wide-potential-window supercapacitors, *Adv. Mater.* 28 (2016) 7680–7687.
- [8] G.F. Chen, Y.Z. Su, P.Y. Kuang, Z.Q. Liu, D.Y. Chen, X. Wu, N. Li, S.Z. Qiao, Polypyrrole shell@3D-Ni metal core structured electrodes for high-performance supercapacitors, *Chem. Eur. J.* 21 (2015) 4614–4621.
- [9] Q. Wang, J. Yan, Z. Fan, Carbon materials for high volumetric performance supercapacitors: design, progress, challenges and opportunities, *Energy Environ. Sci.* 9 (2016) 729–762.
- [10] L. Staaf, P. Lundgren, P. Enoksson, Present and future supercapacitor carbon electrode materials for improved energy storage used in intelligent wireless sensor systems, *Nano Energy* 9 (2014) 128–141.
- [11] M. Yu, Z. Wang, Y. Han, Y. Tong, X. Lu, S. Yang, Recent progress in the development of anodes for asymmetric supercapacitors, *J. Mater. Chem. A* 4 (2016) 4634–4658.
- [12] X. Xiao, X. Peng, H. Jin, T. Li, C. Zhang, B. Gao, B. Hu, K. Huo, J. Zhou, Freestanding mesoporous vn/cnt hybrid electrodes for flexible all-solid-state supercapacitors, *Adv. Mater.* 25 (2013) 5091–5097.
- [13] X. Lu, M. Yu, T. Zhai, G. Wang, S. Xie, T. Liu, C. Liang, Y. Tong, Y. Li, High energy density asymmetric quasi-solid-state supercapacitor based on porous vanadium nitride nanowire anode, *Nano Lett.* 13 (2013) 2628–2633.
- [14] P. Yang, Y. Ding, Z. Lin, Z. Chen, Y. Li, P. Qiang, M. Ebrahimi, W. Mai, C.P. Wong, Z.L. Wang, Low-cost high-performance solid-state asymmetric supercapacitors based on MnO₂ nanowires and Fe₂O₃ nanotubes, *Nano Lett.* 14 (2014) 731–736.
- [15] K. Karthikeyan, S. Amaresh, S.N. Lee, V. Aravindan, Y.S. Lee, Fluorine-doped Fe₂O₃ as high energy density electroactive material for hybrid supercapacitor applications, *Chem. Asian J.* 9 (2014) 852–857.
- [16] X.-F. Lu, X.-Y. Chen, W. Zhou, Y.-X. Tong, G.-R. Li, α-Fe₂O₃@PANI core-shell nanowire arrays as negative electrodes for asymmetric supercapacitors, *ACS Appl. Mater. Interfaces* 7 (2015) 14843–14850.
- [17] Z. Ma, X. Huang, S. Dou, J. Wu, S. Wang, One-pot synthesis of Fe₂O₃ nanoparticles on nitrogen-doped graphene as advanced supercapacitor electrode materials, *J. Phys. Chem. C* 118 (2014) 17231–17239.
- [18] X. Tang, R. Jia, T. Zhai, H. Xia, Hierarchical Fe₃O₄@Fe₂O₃ core-shell nanorod arrays as high-performance anodes for asymmetric supercapacitors, *ACS Appl. Mater. Interfaces* 7 (2015) 27518–27525.
- [19] D. Wang, Y. Li, Q. Wang, T. Wang, Nanostructured Fe₂O₃-graphene composite as a novel electrode material for supercapacitors, *J. Solid State Electrochem.* 16 (2012)

- 2095–2102.
- [20] L. Wang, H. Yang, X. Liu, R. Zeng, M. Li, Y. Huang, X. Hu, Constructing hierarchical tectorum-like $\alpha\text{-Fe}_2\text{O}_3/\text{PPy}$ nanoarrays on carbon cloth for solid-state asymmetric supercapacitors, *Angew. Chem.* 129 (2017) 1125–1130.
 - [21] X. Lu, Y. Zeng, M. Yu, T. Zhai, C. Liang, S. Xie, M.S. Balogun, Y. Tong, Oxygen-deficient hematite nanorods as high-performance and novel negative electrodes for flexible asymmetric supercapacitors, *Adv. Mater.* 26 (2014) 3148–3155.
 - [22] R.H. Hansen, H. Schonhorn, A new technique for preparing low surface energy polymers for adhesive bonding, *J. Polym. Sci. Part C: Polym. Lett.* 4 (1966) 203–209.
 - [23] P.K. Chu, J. Chen, L. Wang, N. Huang, Plasma-surface modification of biomaterials, *Mater. Sci. Eng. R: Rep.* 36 (2002) 143–206.
 - [24] E. Liston, L. Martinu, M. Wertheimer, Plasma surface modification of polymers for improved adhesion: a critical review, *J. Adhes. Sci. Technol.* 7 (1993) 1091–1127.
 - [25] Y. Park, S. Tasaka, N. Inagaki, Surface modification of tetrafluoroethylene-hexafluoropropylene (FEP) copolymer by remote H_2 , N_2 , O_2 , and Ar plasmas, *J. Appl. Polym. Sci.* 83 (2002) 1258–1267.
 - [26] Y. Park, N. Inagaki, Surface modification of poly (vinylidene fluoride) film by remote Ar, H_2 , and O_2 plasmas, *Polymer* 44 (2003) 1569–1575.
 - [27] L. Xu, Q. Jiang, Z. Xiao, X. Li, J. Huo, S. Wang, L. Dai, Plasma-engraved Co_3O_4 nanosheets with oxygen vacancies and high surface area for the oxygen evolution reaction, *Angew. Chem.* 128 (2016) 5363–5367.
 - [28] S. Dou, C.L. Dong, Z. Hu, Y.C. Huang, J. Chen, L. Tao, D. Yan, D. Chen, S. Shen, S. Chou, Atomic-scale CoO_x species in metal-organic frameworks for oxygen evolution reaction, *Adv. Funct. Mater.* 27 (2017).
 - [29] Y. Wang, Y. Zhang, Z. Liu, C. Xie, S. Feng, D. Liu, M. Shao, S. Wang, Layered double hydroxide nanosheets with multiple vacancies obtained by dry exfoliation as highly efficient oxygen evolution electrocatalysts, *Angew. Chem. Int. Ed.* 56 (2017) 5867–5871.
 - [30] B. Ouyang, Y. Zhang, Z. Zhang, H.J. Fan, R.S. Rawat, Nitrogen-plasma-activated hierarchical nickel nitride nanorods for energy applications, *Small* 13 (2017).
 - [31] B. Ouyang, Y. Zhang, Y. Wang, Z. Zhang, H.J. Fan, R.S. Rawat, Plasma surface functionalization induces nanostructuring and nitrogen-doping in carbon cloth with enhanced energy storage performance, *J. Mater. Chem. A* 4 (2016) 17801–17808.
 - [32] Y. Zhang, R.S. Rawat, H.J. Fan, Plasma for rapid conversion reactions and surface modification of electrode materials, *Small Methods* 1 (2017) 1700164.
 - [33] Y. Zhang, B. Ouyang, J. Xu, S. Chen, R.S. Rawat, H.J. Fan, 3D porous hierarchical nickel-molybdenum nitrides synthesized by RF plasma as highly active and stable hydrogen-evolution-reaction electrocatalysts, *Adv. Energy Mater.* 6 (2016) 1600221.
 - [34] Y. Zhang, B. Ouyang, J. Xu, G. Jia, S. Chen, R.S. Rawat, H.J. Fan, Rapid synthesis of cobalt nitride nanowires: highly efficient and low-cost catalysts for oxygen evolution, *Angew. Chem. Int. Ed.* 55 (2016) 8670–8674.
 - [35] G. Wang, T. Ogawa, M. Umeno, T. Soga, T. Jimbo, Surface and bulk passivation of gas solar cell on Si substrate by $\text{H}_2 + \text{PH}_3$ plasma, *Appl. Phys. Lett.* 76 (2000) 730–732.
 - [36] H. Liang, A.N. Gandi, D.H. Anjum, X. Wang, U. Schwingenschlög, H.N. Alshareef, Plasma-assisted synthesis of NiCoP for efficient overall water splitting, *Nano Lett.* 16 (2016) 7718–7725.
 - [37] H. Liang, A.N. Gandi, C. Xia, M.N. Hedhili, D.H. Anjum, U. Schwingenschlög, H.N. Alshareef, Amorphous NiFe-OH/NiFeP electrocatalyst fabricated at low temperature for water oxidation applications, *ACS Energy Lett.* 2 (2017) 1035–1042.
 - [38] H. Liang, C. Xia, Q. Jiang, A.N. Gandi, U. Schwingenschlög, H.N. Alshareef, Low temperature synthesis of ternary metal phosphides using plasma for asymmetric supercapacitors, *Nano Energy* 35 (2017) 331–340.
 - [39] H. Liang, H.N. Alshareef, A plasma-assisted route to the rapid preparation of transition-metal phosphides for energy conversion and storage, *Small Methods* 1 (2017) 1700111.
 - [40] P. Jiang, Q. Liu, Y. Liang, J. Tian, A.M. Asiri, X. Sun, A cost-effective 3D hydrogen evolution cathode with high catalytic activity: FeP nanowire array as the active phase, *Angew. Chem. Int. Ed.* 53 (2014) 12855–12859.
 - [41] L. Lutterotti, S. Matthies, H.R. Wenk, Maud: a friendly java program for material analysis using diffraction, *IUCr: Newl. CPD* 21 (1999) 14–15.
 - [42] Z. Wu, B. Li, Y. Xue, J. Li, Y. Zhang, F. Gao, Fabrication of defect-rich MoS_2 ultrathin nanosheets for application in lithium-ion batteries and supercapacitors, *J. Mater. Chem. A* 3 (2015) 19445–19454.
 - [43] A. Grosvenor, B. Kobe, M. Biesinger, N. McIntyre, Investigation of multiplet splitting of Fe 2p XPS spectra and bonding in iron compounds, *Surf. Interface Anal.* 36 (2004) 1564–1574.
 - [44] T. Yamashita, P. Hayes, Analysis of XPS spectra of Fe^{2+} and Fe^{3+} ions in oxide materials, *Appl. Surf. Sci.* 254 (2008) 2441–2449.
 - [45] Y. Yan, L. Thia, B.Y. Xia, X. Ge, Z. Liu, A. Fisher, X. Wang, Construction of efficient 3D gas evolution electrocatalyst for hydrogen evolution: porous FeP nanowire arrays on graphene sheets, *Adv. Sci.* 2 (2015) 1500120.
 - [46] G. Alvarez, R. Font, J. Portelles, O. Raymond, R. Zamorano, Paramagnetic resonance and non-resonant microwave absorption in iron niobate, *Solid State Sci.* 11 (2009) 881–884.
 - [47] A. Jitianu, M. Crisan, A. Meghea, I. Rau, M. Zaharescu, Influence of the silica based matrix on the formation of iron oxide nanoparticles in the $\text{Fe}_2\text{O}_3\text{-SiO}_2$ system, obtained by sol-gel method, *J. Mater. Chem.* 12 (2002) 1401–1407.
 - [48] D. Wang, Q. Wang, T. Wang, Controlled synthesis of mesoporous hematite nanostructures and their application as electrochemical capacitor electrodes, *Nanotechnology* 22 (2011) 135604.
 - [49] M.B. Sassin, A.N. Mansour, K.A. Pettigrew, D.R. Rolison, J.W. Long, Electroless deposition of conformal nanoscale iron oxide on carbon nanoarchitectures for electrochemical charge storage, *ACS Nano* 4 (2010) 4505–4514.
 - [50] L.-F. Chen, Z.-Y. Yu, X. Ma, Z.-Y. Li, S.-H. Yu, In situ hydrothermal growth of ferric oxides on carbon cloth for low-cost and scalable high-energy-density supercapacitors, *Nano Energy* 9 (2014) 345–354.
 - [51] H. Liang, F. Meng, M. Cabán-Acevedo, L. Li, A. Forticaux, L. Xiu, Z. Wang, S. Jin, Hydrothermal continuous flow synthesis and exfoliation of NiCo layered double hydroxide nanosheets for enhanced oxygen evolution catalysis, *Nano Lett.* 15 (2015) 1421–1427.
 - [52] H. Liang, L. Li, F. Meng, L. Dang, J. Zhuo, A. Forticaux, Z. Wang, S. Jin, Porous two-dimensional nanosheets converted from layered double hydroxides and their applications in electrocatalytic water splitting, *Chem. Mater.* 27 (2015) 5702–5711.
 - [53] C. Liu, C. Zhang, H. Fu, X. Nan, G. Cao, Exploiting high-performance anode through tuning the character of chemical bonds for Li-ion batteries and capacitors, *Adv. Energy Mater.* 7 (2017) 1601127.
 - [54] J. Zhao, S. Wang, Z. Run, G. Zhang, W. Du, H. Pang, Hydrothermal synthesis of nickel phosphate nanorods for high-performance flexible asymmetric all-solid-state supercapacitors, *Part. Syst. Charact.* 32 (2015) 880–885.
 - [55] H. Pang, S. Wang, W. Shao, S. Zhao, B. Yan, X. Li, S. Li, J. Chen, W. Du, Few-layered $\text{CoHPO}_4 \cdot 3\text{H}_2\text{O}$ ultrathin nanosheets for high performance of electrode materials for supercapacitors, *Nanoscale* 5 (2013) 5752–5757.
 - [56] H. Pang, Y. Liu, J. Li, Y. Ma, G. Li, Y. Ai, J. Chen, J. Zhang, H. Zheng, Cobalt phosphite microarchitectures assembled by ultralong nanoribbons and their application as effective electrochemical capacitor electrode materials, *Nanoscale* 5 (2012) 503–507.
 - [57] J.F. Callejas, J.M. McEnaney, C.G. Read, J.C. Crompton, A.J. Bicchieri, E.J. Popczun, T.R. Gordon, N.S. Lewis, R.E. Schaak, Electrocatalytic and photocatalytic hydrogen production from acidic and neutral-pH aqueous solutions using iron phosphide nanoparticles, *ACS Nano* 8 (2014) 11101–11107.
 - [58] J. Tian, Q. Liu, Y. Liang, Z. Xing, A.M. Asiri, X. Sun, FeP nanoparticles film grown on carbon cloth: an ultrahighly active 3D hydrogen evolution cathode in both acidic and neutral solutions, *ACS Appl. Mater. Interfaces* 6 (2014) 20579–20584.
 - [59] Q. Lv, K. Chi, Y. Zhang, F. Xiao, J. Xiao, S. Wang, K.P. Loh, Ultrafast charge/discharge solid-state thin-film supercapacitors via regulating the microstructure of transition-metal-oxide, *J. Mater. Chem. A* 5 (2017) 2759–2767.
 - [60] A. Shanmugavani, R.K. Selvan, Synthesis of ZnFe_2O_4 nanoparticles and their asymmetric configuration with Ni(OH)_2 for a pseudocapacitor, *RSC Adv.* 4 (2014) 27022–27029.
 - [61] Y. Wang, C. Shen, L. Niu, R. Li, H. Guo, Y. Shi, C. Li, X. Liu, Y. Gong, Hydrothermal synthesis of $\text{CuCo}_2\text{O}_4/\text{CuO}$ nanowire arrays and $\text{rGO}/\text{Fe}_2\text{O}_3$ composites for high-performance aqueous asymmetric supercapacitors, *J. Mater. Chem. A* 4 (2016) 9977–9985.
 - [62] L. Zhu, Z. Chang, Y. Wang, B. Chen, Y. Zhu, W. Tang, Y. Wu, Core-shell $\text{MnO}_2@ \text{Fe}_2\text{O}_3$ nanospindles as a positive electrode for aqueous supercapacitors, *J. Mater. Chem. A* 3 (2015) 22066–22072.
 - [63] A. Mahmood, R. Zou, Q. Wang, W. Xia, H. Tabassum, B. Qiu, R. Zhao, Nanostructured electrode materials derived from metal-organic framework xerogels for high-energy-density asymmetric supercapacitor, *ACS Appl. Mater. Interfaces* 8 (2016) 2148–2157.
 - [64] A.M. Khattak, H. Yin, Z.A. Ghazi, B. Liang, A. Iqbal, N.A. Khan, Y. Gao, L. Li, Z. Tang, Three dimensional iron oxide/graphene aerogel hybrids as all-solid-state flexible supercapacitor electrodes, *RSC Adv.* 6 (2016) 58994–59000.
 - [65] W.-H. Jin, G.-T. Cao, J.-Y. Sun, Hybrid supercapacitor based on MnO_2 and columned FeOOH using Li_2SO_4 electrolyte solution, *J. Power Sources* 175 (2008) 686–691.
 - [66] K. Karthikeyan, D. Kalpana, S. Amareesh, Y.S. Lee, Microwave synthesis of graphene/magnetite composite electrode material for symmetric supercapacitor with superior rate performance, *RSC Adv.* 2 (2012) 12322–12328.
 - [67] T. Brousse, D. Bélanger, A hybrid $\text{Fe}_3\text{O}_4\text{-MnO}_2$ capacitor in mild aqueous electrolyte, *Electrochem. Solid-State Lett.* 6 (2003) A244–A248.

Hanfang Liang received his Ph.D. in applied chemistry in 2015 from Xiamen University. As a visiting graduate student, he studied at University of Wisconsin-Madison from 2013 to 2015. He is currently a postdoc in Prof. Husam Alshareef's group at KAUST. His current research focuses on rational growth of nanomaterials and their applications.





Chuan Xia is currently a Ph.D. candidate of the Materials Science and Engineering program at KAUST. His research interests focus on the development of nanostructured chalcogenides and their applications.



Xiaohe Miao received a Ph.D. Degree from Zhejiang University and was a postdoctoral fellow in KAUST Catalysis Center in 2010–2014. Currently she is staff scientist in Imaging and Characterization Core Lab of KAUST. Her research interests focus on the design, synthesis and structure determination of metal-organic frameworks (MOFs) for the applications of heterogeneous/homogeneous catalysis, gas separation and energy storage/conversion.



Abdul-Hamid Emwas received a M.Sc. in Biophysical Chemistry University of Bergen and a Ph.D. in Physical Chemistry from University of New Brunswick. Currently he is a research scientist at NMR Core Lab of KAUST. Before that he worked at the Miami University, USA, CRUK Institute for Cancer Studies, and University of Waterloo.



Husam N. Alshareef is a Professor of Materials Science & Engineering at King Abdullah University of Science & Technology (KAUST). He obtained his Ph.D. at North Carolina State University, USA. Following nearly 10 years of experience in the semiconductor industry, he joined KAUST in 2009. His group is interested in developing semiconductor nanomaterials for electronics and energy applications.



Dalaver H. Anjum received his Ph.D. Physics in 2002 from the University at Albany-State University of New York. Currently he is a Sr. Scientist in the Imaging and Characterization Lab of KAUST. In this capacity, he is performing materials characterization by utilizing TEM. He performs the imaging, diffraction, elemental analyses of materials to determine their structure-property relationships. He has authored/co-authored over 180 publications related to the field of materials characterization by using TEM.